recycling

MDPI

Article

Advancing Real-Time Sensor-Based Quality Monitoring in Construction and Demolition Waste Processing for the Prediction of Weight-Based Particle Size Distributions

Lieve Göbbels *, Karoline Raulf, Setenay Orbatu and Kathrin Greiff

Department of Anthropogenic Material Cycles, RWTH Aachen University, Wüllnerstraße 2, 52062 Aachen, Germany
* Correspondence: lieve.goebbels@ants.rwth-aachen.de

Abstract

In this work, the development and validation of an AI- and sensor-based inline quality monitoring system for the analysis of particle size distributions (PSDs) of comminuted construction and demolition waste (CDW) material flows are described. In this, a custom-developed multitask CNN (CDW-MT-CNN) was developed using manually sieve analyzed particles. This model is able to rapidly and simultaneously predict the particle class and weight, essential for the determination of the PSD. The single particle data are then aggregated per raw image, usually consisting of around 1000 particles for full-scale experiments, to acquire a per-image PSD. The inline mounted RGB line scan sensor records high-resolution images in subsecond frequencies. With an inference time of around 54 ms for a single image, this model would be able to provide a PSD every minute in a full-scale plant. For the purpose of inline monitoring of CDW material flows in a comminution process, such intervals are sufficient according to experts and solve existing gaps regarding the upscaling of laboratory-developed systems. Together with the high predictive performance of the model, especially in terms of classification (82% accuracy), it is shown that this technology has potential for monitoring in full-scale plants, for instance by offering operators new insights to improve operation efficiency. Further research should focus on increasing the precision for weight prediction, for instance by increasing the labeled data set with a larger number of unique particles and on methods to verify the performance of the model on pilot or full-scale plants during live operation.

Keywords: multitask-CNN; 2D-based material characterization; particle size distribution; construction and demolition waste; inline sensor-based material flow characterization; recycled concrete aggregates

Check for updates

Academic Editor: Michele John

Received: 31 March 2026
Revised: 22 May 2026
Accepted: 28 May 2026
Published: 1 June 2026

Copyright: © 2026 by the authors. Licensee MDPI, Basel, Switzerland. This article is an open access article distributed under the terms and conditions of the Creative Commons Attribution (CC BY) license.

1. Introduction

Across the European continent, trends indicating increasing demands for construction and building materials are visible, rendering innovations for the improvement of material sustainability within the construction sector—in particular regarding high-grade recycling—a European concern [1,2]. In Germany, the increase in the number of building permits for residential construction in 2020 (+2.2%) and 2021 (+4.8%) [3], renovation of 40,000 dwellings by 2026 [4] and the government's goal to build 400,000 new dwellings annually [5] show the considerable potential for increased high-grade use of recycled CDW materials. Given that in 2022 nearly 24 million tons of construction and demolition waste

(CDW) were generated and forwarded to Germany's 2.676 CDW processing facilities [6], corresponding to approximately 30 wt% of the generated CDW from Germany's construction sector [1], a considerable material stream for the production of high-quality recycled aggregates is already established, but further potential exists in increasing the amount of material being recycled.

To this day, however, monitoring the quality of the material in CDW processing remains a procedure reliant on manual sampling, despite the inherent lack of transparency regarding material specifications and the material stream characteristics that occur due to limitations of manual sampling. Nonetheless, in recent years, there has been an increasing interest in automating material specification analyses, for instance as a basis for assessing the usability of CDW recycled aggregates as a substitute for primary raw materials in high-quality applications such as structural engineering [7] and road construction [8]. In a previous study, we found that research on automating material specification analyses in CDW processing is mostly focused on material characterization, e.g., to sort out contaminants, and mainly takes place on lower technology readiness levels (TRLs) [9]. The latter is among other things due to a general lack of labeled data needed for the development of supervised deep learning architectures, the lack of testing in realistic environments and, related to this, the complexity of CDW material streams. Additionally, similar to other waste streams (e.g., [10]), several quality factors on the particle or material flow level are based on the weight of the particle or flow, which is difficult to extract from 2D-based sensor data [11]. Alternatively, the use of 3D sensing technologies, such as 3D-laser triangulation, could be used [12–14], but given the severe economic constraints and rough environments concerning CDW processing [15–17], this currently remains practically infeasible.

To improve the use of CDW recycled aggregates in high-quality applications by increasing the transparency of the material specifications during processing while keeping the costs of the automation technology low, a combination of 2D sensing and deep learning appears to be a suitable strategy for the development of an inline quality monitoring technology. Such a technology can have several benefits compared to the manual procedure that is currently used, including higher transparency and data richness required for detailed and therewith more trustworthy certification, which could incentivize the use of higher rates of recycled aggregates in construction. Moreover, the increased transparency in combination with real-time results would allow plant operators to efficiently adjust operating parameters to maximize the quality of the produced recyclates, allowing use in a wider and qualitatively higher range of application areas. CDW recycled aggregates are validated by a set of quality factors, ranging from geometrical to chemical indicators, which vary depending on the intended application (e.g., DIN EN 12620 and DIN EN 13285 [18,19]). Moreover, the importance and usage of the quality factors differ across countries. In Germany, the weight-based PSD is one of the primary quality indicators for CDW processing companies. In this context, thus, the particle size distribution (PSD) seems to be one of the most appropriate quality factors to investigate: not only is it one of several essential indicators of the CDW material quality, but it also partially comprises 2D data that can be extracted using 2D sensing technologies. That is, the particle size distribution represents the cumulative weight percentage of particles classified by their size. However, this still means that, based on the 2D particle class data, an accurate approximation of the weight needs to be made. In the context of CDW, this remains an unsolved problem to this day [20].

1.1. Related Work

Complementary metal-oxide-semiconductor (CMOS) optical sensors recording 2D RGB data—also referred to as RGB cameras—have already shown promising results for

primary materials such as glass bead characterization on a µm scale [21] and solids during air flow-based transportation in pipes [22]. A first approach for the particle size classification of CDW material was provided by Di Maria et al. in 2016, who proposed and implemented a so-called 'look-up catalogue' procedure [11]. This procedure is, however, not directly applicable for in- or online quality monitoring during processing because of the lack of a real-time recording and analysis system, but it could be used as a baseline, given a sufficient number of mixture scenarios and different size distributions are provided. Similar to the look-up catalogue procedure, particle analyzers exist and are able to provide good results but are not suitable for inline quality monitoring systems in rough CDW comminution environments. Laser diffraction is frequently used in determining the PSD of soils or sediments, providing a volume-based distributions of particles up to 2 mm [23].

In a previous study [12], we investigated the potential of using 3D-laser triangulation (3DLT)-based grayscale images of individual CDW particles to train existing and custom CNN architectures for the prediction of the volume-based PSD. The best models are custom architectures specially designed for the task and are able to achieve an overall classification of the particle size of 79.6% and 78.9%, respectively. Additionally, aggregating the classifications with the predicted volume to a cumulative volume-based PSD shows only minor deviations from the true cumulative volume of the independent test set. So, this work shows promising results of in particular custom-built CNN architectures to classify particles according to their particle size class and extract information about the particle's volume, which is embedded in the pixel intensity, i.e., the grayscale. However, this work contains three main limitations for practical applicability: (1) this study focuses on volume-based predictions, wherein features can be extracted from the 3DLT-based greyscale images, but commonly used norms in Germany and other European countries require mass- or weight-based PSDs. This requirement furthermore limits the usability of standard computer vision techniques such as classic particle measuring, especially in the context of inline monitoring; (2) even though the performance is promising, the developed architectures are heavy-weight and lead to slow inference times; and (3) investigations from other researchers thus far indicate limited applicability of the 3DLT sensor technology in the CDW processing industry due to high costs and low robustness [15,16], which was confirmed in our own practical assessments [17,24].

Furthermore, as indicated in the work by Di Maria et al., having sufficient labeled data is imminent for good predictive performance but time-consuming and costly for CDW given the large variety of particles in terms of sizes, shapes and material compositions. As such, to this day, no large and labeled data sets for (single) CDW particles exist that could be used for the training of deep learning models for the prediction of the PSD. However, some approaches to the limitations of acquiring suitable CDW image data have been proposed. For instance, Kronenwett et al. [25] describe how synthetic data with different occlusion rates can be created using two distinct types of particles: instances of brick and sand-lime stone. Additionally, Beskopylny et al. [26] use data augmentation to increase the limited data set of 45 photographed particles and train models for the classification of particle shape.

1.2. Aims and Research Questions

In this work, we investigate a possible solution for existing limitations regarding sensor-based quality monitoring for CDW, in particular inline monitoring of the (weight-based) PSD. Especially fast enough inference time through lightweight architecture development and the prediction of the particles' weight from RGB image data—instead of data containing 3D information—are the main focus of this feasibility study. More specifically, the relevance of this work is two-fold. On the one hand, we adapt a CNN-approach—

namely the multitask-CNN approach—not previously used in waste management to predict the weight-based PSD in the context of inline quality monitoring. With this, we provide a first attempt at solving the problem of translating 2D information to weight data for particles where no standard material density can be assumed. On the other hand, we aim to mitigate large gaps that exist between models developed on a laboratory scale and the actual practical prerequisites by adapting a bottom-up approach of using practical experiences for the development of a model that is in its basis implementable in real CDW processing environments. As such, we also tested the model using full-scale plant data and described resulting implications. Correspondingly, in this work, the following two research questions will be answered:

RQ1: To what extent can particle size classes and particle weight using only a limited set of 2D-RGB data be predicted with sufficient efficiency, both regarding speed and predictive performance, to meet the practical requirements for the CDW comminution process?
RQ2: How does the proposed solution from **RQ1** perform as part of the developed quality monitoring system when applied on full-scale plant data, and what are the implications for a full-fledged implementation in a full-scale plant?

2. Materials and Methods

2.1. Materials and Sample Preparation

2.1.1. Sampling Campaign

In order to develop the quality monitoring system and corresponding experiments, acquisition of real CDW material is necessary. Given the heterogeneity of CDW, we conducted multiple sampling campaigns, separated by long time frames (i.e., 4–6 months between each campaign) at the same processing plant from MAV Krefeld GmbH,located in North Rhine-Westphalia, Germany. The first sampling campaigns were of an exploratory nature, where the focus was on gaining a first idea of the material composition. Subsequently, a minor sampling campaign was conducted specifically to acquire proper material quantities with realistic compositions. Next, given the high importance but small proportion of large-sized particles, additional material—selected by hand from the processed material collection at the full-scale plant to acquire mostly large particles—acquisition was undertaken. In total, around 500 kg of unbound comminuted recycled concrete (RC) mixture has been sampled specifically for laboratory experiments and analysis. This RC mixture consists mainly of concrete but also contains bricks, tiles and steel reinforcements (as can be seen in Figure 1a), as well as a small share of contaminants such as textiles, plastics and glass. In Figure 1b, an example of the material after comminution and sieve analysis is shown. In the processed, i.e., sieved, material, remaining plastic and textile as well as steel contaminants are taken out, as these are in principle separated from the stream by a wind sifter and overbelt magnetic separator before the inline data recording location is reached.

To acquire full-scale plant data to perform a first validation of the model's performance on full-scale imaging data, another sampling campaign was conducted. Here, samples were taken with a duration of 1 to 3 s, depending on the throughput of the fine grain conveyor at the end of the mobile impact crusher. Additionally, time stamps and other metadata were recorded for each individual sample to later match the sample's sieve results to the image(s) recorded at the same point in time. In this study, the samples of two experiments are used, totaling 84 kg and 11 corresponding high-resolution images.



(**a**) (**b**)

Figure 1. (**a**) Raw, non-comminuted input material. (**b**) Material after comminution and sieve analysis.

2.1.2. Classification Procedure

As the focus is on the particle size distribution as a quality factor of the geometric characteristics of CDW, corresponding to, e.g., DIN EN 13242 [27], analysis procedures according to the different guiding norms have been conducted to determine the ground truths. First, according to DIN EN 933-1, material was dried in a dehumidifier at 85 degrees Celsius until weight constancy [28]. This temperature was chosen to avoid potential contaminants, especially plastic foils, from melting and therewith compromising the sample. The dried samples were then analyzed using the procedure described in DIN EN 933-1 for the target product unbound RC mixture, $G_{B,\,0/45}$ [19,28]. Accordingly, a large laboratory analysis sieve was used to classify the samples in terms of their particle sizes, i.e., to determine the particle size class for each particle and to determine the percent by weight (wt%) for each class of the sample. Previous testing empirically showed suitable fill levels and sieve duration [29]. As such, around 15 L of sample material was sieved at a time with a duration of 90 s. Classified material was then deposited and stored in labeled buckets according to its particle size class. Conforming to DIN EN 13285 [19]and the procedure conducted by laboratory personnel at the partner processing plant, screens with undersizes 0.5 mm, 1 mm, 2 mm, 5.6 mm, 11.2 mm and 22.4 mm were used as main screens, but screens with undersizes 0.063 mm, 4 mm, 8 mm, 16 mm, 31.5 mm, 45 mm and 63 mm were added as additional sieves to avoid clogging and increase the amount of information that can be retrieved for adjustment of operation procedures [19,28].

2.2. Methods

2.2.1. Laboratory Analysis and Data Acquisition

Particles from each class, ranging between 2 mm and 63 mm, were weighed and photographed with similar spatial resolution, as the configured JAI (Copenhagen, Denmark) SW-8000T line scan RGB sensor and the results were documented based on the particle's uniquely assigned label. Additionally, the acquired weights and particle counts were analyzed for each class to gain insights into the weight fluctuations when randomly picking particles from the different classes and to assess the skewness of the number of particles across the classes. In total, 1486 particles were captured and analyzed to acquire a mostly balanced data set. Note that there are few particles for the class 2 to 4 mm. This is due to the particles being too light (i.e., less than 1 mg) for the available scales and not identifiable by the segmentation model implemented in the quality monitoring system (see Section 2.2.5). As such, after testing 16 particles, it was decided to instead focus on the other particle size classes. Nonetheless, this class is considered in this work as it functions as the edge case:

the biggest particles in this class could still be segmented and processed by the models. It is thus worthwhile investigating the predictability, even though merely 16 particles are included and it is not a main focus of this work. In Table 1, the number of particles for each class is shown, further including the mean and standard deviations. As the data in the table indicate, there are stark deviations between the weights even within the respective particle classes, which can be explained by the high variability of materials and their characteristics embedded in mixed CDW [30].

Table 1. Number of particles recorded and used in the data set for each class.

Class (mm)	Nr. Particles (-)	Particle Weight (g) $\mu \pm \sigma$
2–4	16	0.051 ± 0.033
4–5.6	260	0.118 ± 0.045
5.6–8	200	0.428 ± 0.219
8–11.2	199	1.197 ± 0.455
11.2–16	200	3.256 ± 1.437
16–22.4	200	8.368 ± 3.808
22.4–31.5	157	28.468 ± 15.919
31.5–45	103	73.059 ± 24.618
45–63	151	98.875 ± 42.300

2.2.2. Data Pre-Processing

After photographing each particle, particles were segmented using Python's standard computer vision and segmentation tools (Python 3.12) and were manually assessed for correctness. Additionally, a 225 by 225 pixels black background was added to each particle after downscaling the resolution of each particle to match the resolution after the segmentation process in the quality monitoring system (see Section 2.2.5), which is performed to ensure faster training and inference processes. Furthermore, given that multiple tasks need to be solved by the model in parallel, a multitask data set was created, leveraging the unique labels to link both the particle's class and its weight to the corresponding image.

Given the high variance in terms of particle weights, however, we assume significant limitations exist when using solely this 'original' data set for training CNN-based models, as the combination of diversity and the size of the data set are the most important factors that lead to high model performance. If the model does not observe different forms and a large enough variety of samples, it cannot improve itself in terms of extracting essential but generalizable patterns. Such models can easily overfit the training data [31], capturing only the exact characteristics of certain items that are not applicable to other items. However, collecting sufficient data is both time-consuming and costly. As a solution to the limited data set we acquired for this work, we also applied data augmentation as a technique to synthetically increase the heterogeneity of the training set by (randomly) modifying existing samples or creating new ones [32,33] therewith intending to increase the robustness and accuracy of the models and allowing them to perform well on small, poorly representative data [34]. Before applying augmentation techniques to the data, 300 samples were saved separately using stratified random sampling to create an unseen test set, resulting in a training set of 1186 original images. Additionally, the data set extended with augmentations is saved and used as a separate data set. That is, each model training procedure is performed twice under otherwise identical conditions: once on the original data set without any augmentations and once on the augmented or extended data set.

To create the extended data set, three main augmentations (t_1 to t_3) have been applied to the images in the training set. To protect the physical features of the samples and

create a data set that allows developing models that are more robust to the real-world (i.e., full-scale plant) data, augmentation methods were selected accordingly. Adjustments like permutations, noise injection and pixel value transformations operationally diversify data without changing semantics [35]. It is important for samples to preserve their original class label and maintain a similar weight. To do so, the same class label was added to the augmented image based on its source image, and the true weight was varied randomly with a difference of at most 5%. The latter is performed to avoid overfitting during the training of the weight prediction part but also maintain realistic weight values for each respective particle.

As such, augmentation was restricted to rotation operations with two different angle ranges ($2 \times t_1$), brightness adjustment (t_2) and Gaussian smoothing (t_3), implemented separately and in combination. Rotation (t_1) simulates new rotations and aims to obtain a model that is rotation-invariant. It is considered for two cases: less than 180° and greater than 180° . First, the image is rotated at a random angle between 20° and 160° in the clockwise direction. Then, the second rotation is performed at a random angle between 200° and 340° in the counterclockwise direction, resulting in two augmented sets: particles that are rotated once and those that are rotated twice.

That is, given that the sensor is to be placed in a partially enclosed box on a mobile impact crusher operated outside, it is important to take into account that brightness changes depending on the time of the day and the weather conditions. Brightness adjustment (t_2) plays a crucial role in simulating the different light conditions. A random number is selected between 1.2 and 1.51. This number works as a brightness coefficient and is multiplied with every pixel value of the RGB image.

Similar to the brightness augmentation, t_3 is also based on phenomena occurring in full-scale plants. That is, while samples are transported on the conveyor belts, large vibrations cause motion-blurred images with lower sharpness. Gaussian smoothing takes the average of the pixels and applies a Gaussian smoothing function to reduce the noise of the images. The smoothing coefficient (σ) was chosen randomly between 0.7 and 1.01, where a lower value applies lower amounts of blur and higher levels apply stronger blur. Especially the latter can lead to loss of details regarding the particles' texture. As such, the values were determined based on experiences acquired on a full-scale plant to mimic realistic amounts of blur occurring due to vibrations of the machines. The new data set contains 11,860 images, which is ten times bigger than the original data set.

2.2.3. Model Architecture

The model architecture developed in this work is a custom multitask-CNN named CDW-MT-CNN with a shared backbone and a separate head for each task. The backbone consists of two convolution blocks followed by a dropout layer and another convolution block. Furthermore, the architecture contains two heads: a classification head for the particle size classification and a regression head for the particle weight prediction. Both heads consist of two convolution layers and a dropout layer. Within all sequential blocks, hardswish is used as the activation layer because of the high computational efficiency while leveraging benefits of the ReLU and sigmoid activation functions [36]. With this architecture, there are in total 505,400 trainable parameters given the 225 by 225 pixel input image format. By comparison, AlexNet—an established high-performance CNN-based classification architecture—has 60 million parameters and accepts images with a pixel dimension of 224 by 224 [37]. Other popular CNN models also contain parameters in the range of 7 to 138 million parameters [38–40], which means that, by comparison, the proposed MT-CNN model is a lightweight architecture. Even though a heavier model architecture could provide improved performance, our aim has been to develop a model

that is extremely fast with sufficient prediction. Given that the model would ideally need to process 1200 to 1500 images per second when implemented in a full-scale plant, creating a lightweight and efficient architecture is imminent.

In addition to the necessity for a lightweight architecture, another reason to create a custom model is the lack of suitable models for multitask prediction that could be used for transfer learning on our data set. For instance, Chhapariya et al. [41] published a multitask model to process hyperspectral forestry data, and in [42], a multitask model that predicts the presence of particular brain diseases and quantitative features such as tumor volume based on MRI images was developed. Even though the latter work is relatively close in terms of the type of tasks, the proposed model is extremely deep and considers MRI patches of at most 64 by 64 pixels. To the authors' knowledge, no other multitask models that contain both prediction and classification heads have been published thus far, supporting the development of a new, specialized model for the combined prediction of particle class and weight. Moreover, given that the particle size distribution is just one quality aspect at the basis of high-grade recycling of CDW, the architecture could relatively easily be extended with further heads, for instance, to classify the particles' form, and has potential of being generalized for other domains such as mineralogy.

2.2.4. Model Training and Evaluation

To assess which configuration of hyperparameters leads to the highest performance, each configuration has first been trained using 5-fold cross validation on the training data. This allows assessment of the variation in training results on the basis of five unique divisions of the original training set into a subset of training and validation data, respectively. For each configuration, the average performance over all five folds is taken and used for the final assessment and selection. In addition to variability in the training data that influences a model's performance, we have also used two distinct seeds within the model architecture for a stability test of each configuration. Similarly, each configuration has been applied to both the original as well as the augmented data to allow assessing the influence of using the augmented data set.

The hyperparameters that have been varied are learning rate (1×10^{-5}; 1×10^{-4}; 1×10^{-3}) and the weight of the regression loss (0.1 or 0.2—the loss is divided by 10 to rescale it into the same range as the classification loss) as part of the combined loss and the type of training data (augmented or original). It was decided to use the Adam optimizer (with $\beta_1 = 0.92$, $\beta_2 = 0.997$, and $\epsilon = 1 \times 10^{-8}$) due to the possibility of the optimizer adapting the learning rate during training, making it less susceptible to staying in local optima [43]. In total, 2×12 configurations have been trained and assessed.

The loss function used is a combined loss function based on the cross-entropy loss (CEL; classification) and the Huber loss (regression). CEL is chosen as this loss function takes into account how far away a classification is from the true class. Huber loss is chosen as it is less sensitive to outliers compared to for instance the squared error loss. As such, the implemented loss functions are defined as follows:

$$\begin{aligned} \text{HuberLoss} &= \text{mean}(\ell(x,y) = L = \{l_1, \ldots, l_N\}^T) \\ \text{with } l_n &= \begin{cases} 0.5(x_n - y_n)^2, & \text{if } |x_n - y_n| < 1 \\ 1 \cdot (|x_n - y_n| - 0.5 \cdot 1), & \text{otherwise} \end{cases} \end{aligned} \tag{1}$$

$$\text{CEL} = \ell(x,y) = \sum_{n=1}^{N} \frac{1}{\sum_{n=1}^{N} w_{y_n} \cdot 1\{y_n \neq \text{ignore_index}\}} \cdot l_n \tag{2}$$

where x is the input, y the target, w the weight and N the size of the minibatch dimension.

Additionally, the combined loss was used to avoid overtraining and thus overfitting, where early stopping is initiated if the loss does not improve five epochs in a row.

Furthermore, for the assessment and comparison of the models after partial (K-fold) and final training, the accuracy and Matthews correlation (or phi) coefficient (MCC) were used for the classification performance, and the root mean square error (RMSE) was used to evaluate the weight prediction performance. The main reason for using the MCC in addition to accuracy is the given that MCC is a balanced measure that is insensitive to differences in class sizes and therewith provides an unbiased view of the statistical accuracy [44]. Accuracy, on the other hand, is the standard evaluation metric but is biased—especially when there are class imbalances, as it only regards the number of correct classifications compared the total number of classifications made [45]. Based on these metrics, each model is ranked for the original and stability tested variation. One best model has been selected for each data set variation, meaning that there are two final models: one trained on the original (partial) data and the other on the augmented (partial) data. After selection, both configurations have been retrained on the the seed from the original variation and the complete original and augmented training set, respectively, after which they have been evaluated on the 300 particles of the unseen test set. In addition to the aforementioned metrics, the classification, weight prediction and combined losses as well as the true and predicted value for each instance have been documented. This allows more detailed and flexible performance assessments, for instance, by creating confusion matrices to gain a complete overview of the distribution between true and falsely predicted instances in terms of classification and mean absolute error (MAE). Additionally, saliency maps have been created to investigate what parts of the images underlie the models' predictive decisions. The MAE gives insight into the absolute error independent of the magnitude of the predicted value, therewith providing an unweighted error value that is less influenced by outliers than the RMSE.

2.2.5. Quality Monitoring System

In Figure 2, the complete quality monitoring system is illustrated. Where the focus of this work is on the *particle size distribution prediction* part of the system, *sensor recording* (elaborated in Section 2.2.6) and the *particle segmentation* have been used as a basis for the full-scale plant experiments. For segmentation of the raw images, an adapted version of the ParticleSAM model, proposed in [46], has been implemented. This model takes high-resolution 4096 by 4096 pixel images as input and is able to segment around 1500 particles from 4 mm or bigger (up to >63 mm) per image. As output, the adapted ParticleSAM model used in the current work provides singled-out particles in RGB format on a 225 by 225 pixel background to match the data the CDW-MT-CNN models were trained on.

The CDW-MT-CNN model then takes the segmentation model's output as input and processes it the same way as during inference on the custom-made data set. The classification and weight predictions results for each raw image are stored with the unique GPS label for further analysis. Optionally, the cumulative weight percentage distribution can be forwarded to the next module in the system, but this is out of scope for the current work.

2.2.6. Full-Scale Plant Experiments

In the set-up, the sensor system was constructed with all hardware elements above the fine grain conveyor of a mobile impact crusher, after which several rounds of testing and calibration were conducted. First, the stability and distance of the sensors connected to the aluminum framework were examined and adjusted until appropriate. Next, sensor-specific calibrations were conducted. This included dark signal non-uniformity (DSNU), photo response non-uniformity (PRNU) and gain calibration, as well as data transmission adjustments. For the full-scale experiments, a set conveyor belt frequency was used, and

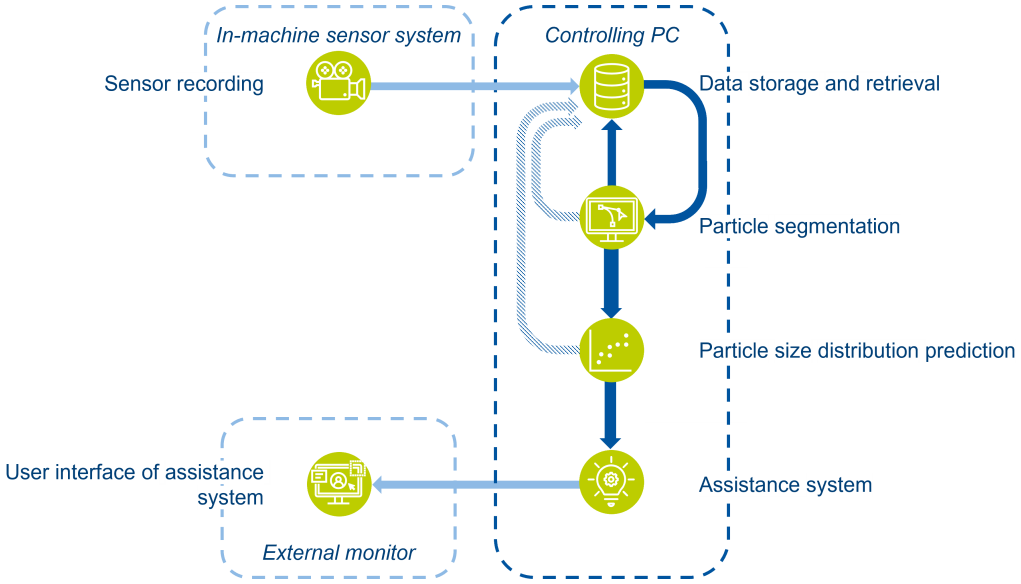


Figure 2. Graphical representation of the used quality monitoring system.

with the help of a built-in tachometer, the speed (constancy) was verified on multiple occasions. The mobile crusher conveyor belt was operated at the standard 20° operation angle and a transportation speed of 1.5 m/s.

Moreover, custom, Python-based recording software was developed to collect all necessary data in the required formats and include all required features for the envisioned experiments and quality monitoring system in general. More specifically, for the recording software, files are always saved with the astropy GPS time stamp (when saving is turned on) to allow time-dimensional comparison and coupling with other data, such as sample (meta)data and machine data. Most of the basic features embedded in the standard delivered software remained in the custom software, such as determining the location in which the data should be saved and the option to live view the latest image. In order to allow a one-to-one comparison of the behavior of the two final CDW-MT-CNNs, it was decided to record the images live while conducting the sampling campaigns but to store these raw images and process them separately by the quality monitoring pipeline for each model. Each image is recorded approximately one second after the previous, and given the line scanning characteristic, the complete material stream is recorded without gaps.

3. Results

3.1. Model Training

In Figure 3, the learning curves of all models in terms of accuracy (classification performance) and RMSE (weight prediction performance) are shown. Here, it can be seen that the models with identical learning rates cluster together, having similar learning durations as well as performance. In general, the models with the largest learning rate (0.001) have the worst accuracy. However, for weight prediction, this is not always the case. That is, model 3 and model 6 achieve the best RMSE for the original and stability test, respectively, compared to the other models also trained on the non-augmented data set.

The best performance averaged over the five folds for each model is shown in Table 2. The models trained on the augmented data set in general seem to classify and predict the weight with high correctness, but it should be noted that some overfitting may have occurred due to large number of augmented images present in the data set. However, even for the models not making use of the augmented data, classification accuracy ranges between 83% and 88%. Similarly, the weight prediction error is relatively constant for these models, ranging between 14.0 g and 12.5 g. Given that the mean weight of the particles

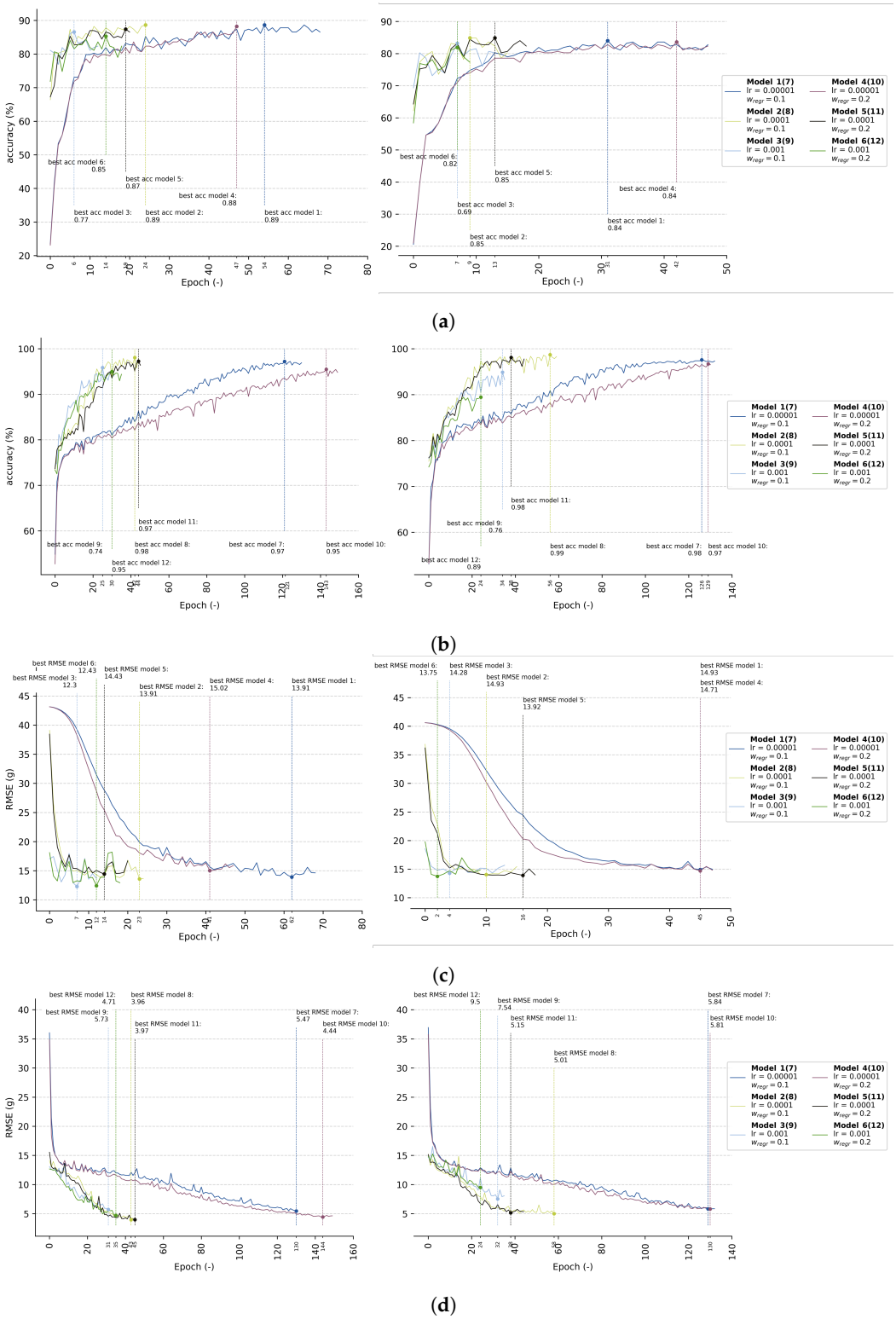


Figure 3. Learning curve for each of the models in terms of accuracy (classification) and RMSE (weight prediction). Abbreviations: lr = learning rate; w_{regr} = weight coefficient of the regression loss. (**a**) Accuracy learning curves of the models trained on the original data using the original seed (left) and the seed used for stability testing (right). (**b**) Accuracy learning curves of the models trained on the augmented data using the original seed (left) and the seed used for stability testing (right). (**c**) RMSE learning curves of the models trained on the original data using the original seed (left) and the seed used for stability testing (right). (**d**) RMSE learning curves of the models trained on the augmented data using the original seed (left) and the seed used for stability testing (right).

in this data set ranges between 1 mg and 104 g (with an overall standard deviation of 35.6 g), this performance is considered sufficient. Based on these results, the configurations from model 2 and model 11 are used for a final retraining on the complete data set and testing on the unseen test data set. Furthermore, after a warm-up phase of 10 iterations, model 2 has a combined (i.e., both weight prediction and classification) inference time of 52.8 ms (average over five rounds of inference) per image for a 16GB NVIDIA RTX 4090 GPU. Similarly, model 11 has an inference time of 54.6 ms on GPU. For CPU, the inference times are 100.8 ms and 76.9 ms, respectively.

Table 2. Average validation accuracy, MCC and RMSE over 5 folds for each model. Bold values indicate the overall best value for the original seed, bold and italicized values indicate the overall best value for the stability tests and italicized values indicate the highest performance for the original seed and stability tests for the models trained on the original data (model 1–6). Models 7–12 regard the augmented data. For accuracy and MCC: the higher the value, the better the performance. For RMSE: the lower the value, the better the performance. Abbreviations: lr = learning rate; w_{regr} = weight coefficient of the regression loss, (s) = stability test.

Model	lr, w_{regr}	Accuracy	MCC	RMSE
Model 1	10^{-6}, 0.1	*0.882*	*0.866*	13.706
Model 1 (s)		0.857	0.836	13.420
Model 2	10^{-5}, 0.1	0.876	0.858	13.317
Model 2(s)		*0.857*	*0.837*	12.580
Model 3	10^{-4}, 0.1	0.838	0.815	13.233
Model 3 (s)		0.838	0.815	13.182
Model 4	10^{-6}, 0.2	0.872	0.853	13.922
Model 4 (s)		0.840	0.817	13.498
Model 5	10^{-5}, 0.2	0.856	0.835	14.031
Model 5 (s)		0.849	0.828	12.614
Model 6	10^{-4}, 0.2	0.842	0.819	*12.499*
Model 6 (s)		0.834	0.811	*12.502*
Model 7	10^{-6}, 0.1	0.970	0.965	5.408
Model 7 (s)		0.976	0.972	5.839
Model 8	10^{-5}, 0.1	**0.985**	**0.983**	4.040
Model 8 (s)		***0.987***	***0.985***	4.681
Model 9	10^{-4}, 0.1	0.964	0.959	4.538
Model 9 (s)		0.961	0.955	5.680
Model 10	10^{-6}, 0.2	0.958	0.952	4.814
Model 10 (s)		0.961	0.955	5.352
Model 11	10^{-5}, 0.2	0.981	0.978	**3.983**
Model 11 (s)		0.985	0.982	***3.881***
Model 12	10^{-4}, 0.2	0.950	0.943	4.712
Model 12 (s)		0.948	0.941	5.124

3.2. Performance on Unseen Data

3.2.1. Classification

To assess the classification performance in an unbiased manner, confusion matrices were analyzed, which can be found in Figure 4. In general, both models are able to classify most particles correctly, acquiring an accuracy of 82% (MCC: 0.80) and 79% (MCC: 0.77) for model 2 and model 11, respectively. These classification results are in line with the classification performance described in our previous study [12], where we trained CNN classifiers on 3DLT-based grayscale images for the prediction of the particle size class.

These particles range from 3.15 mm to 31.5 mm, i.e., have a similar albeit slightly smaller class range. That both models are able to capture and process information from the 2D-RGB images for classification is furthermore indicated by the low number of particles that are classified more than one class distanced from the original class: 4 particles (or 1.3%) for model 2 (see Figure 4a) and 6 particles (or 2.0%) for model 11 (see Figure 4b). When normalizing the number of classified particles based on the true class (see Figure 4c,d), it can be seen that model 2 has an approximately equal (high) performance for particles ranging from 4 to 31.5 mm and that model 11 is more sensitive towards particles in the ranges 5.6 to 11.2 mm and 22.4 to 45 mm. Moreover, both models misclassify larger particles more often, but this behavior is more prominent for model 2 compared to model 11.

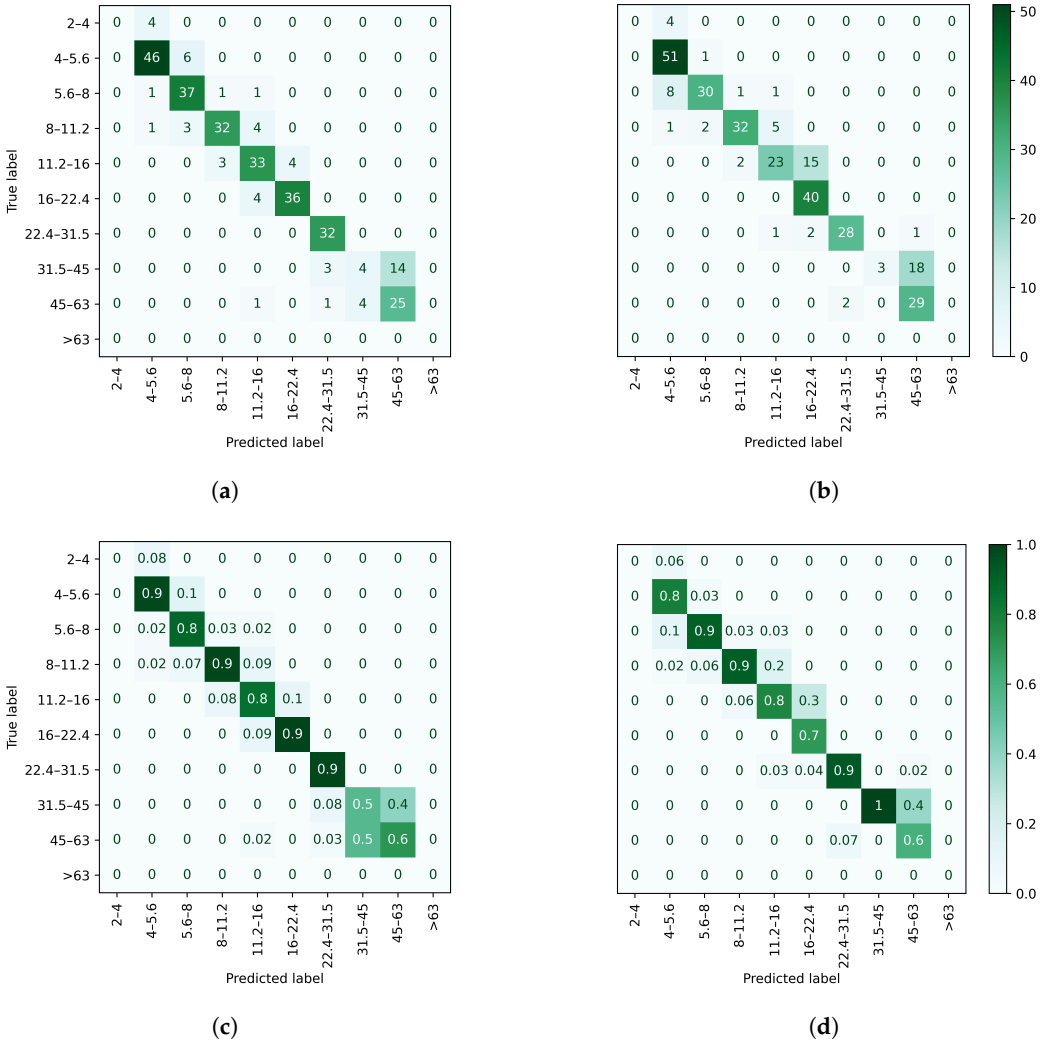


Figure 4. Confusion matrices to visualize the classification performance for the final models. (**a**) Confusion matrix with the number of correctly (diagonal) and falsely (non-diagonal) predicted particles for model 2. (**b**) Confusion matrix with the number of correctly (diagonal) and falsely (non-diagonal) predicted particles for model 11. (**c**) Confusion matrix with the percentage of correctly (diagonal) and falsely (non-diagonal) predicted particles for model 2, normalized based on the true class. (**d**) Confusion matrix with the percentage of correctly (diagonal) and falsely (non-diagonal) predicted particles for model 11, normalized based on the true class.

When looking at the saliency maps of four representative particles used for testing the models' performance (see Figure 5), several things have drawn our attention. First, for small particles, the activation intensity is high in the pixels where the particle is located, whereas for larger—and especially the largest—particles, the area and background around the particle have high intensity but not the pixels representing the particle. Second, for

model 11, more pixels have high activation intensity except for the smallest particles, which could explain the poorer performance of this model on classifying the smallest classes compared to model 2.

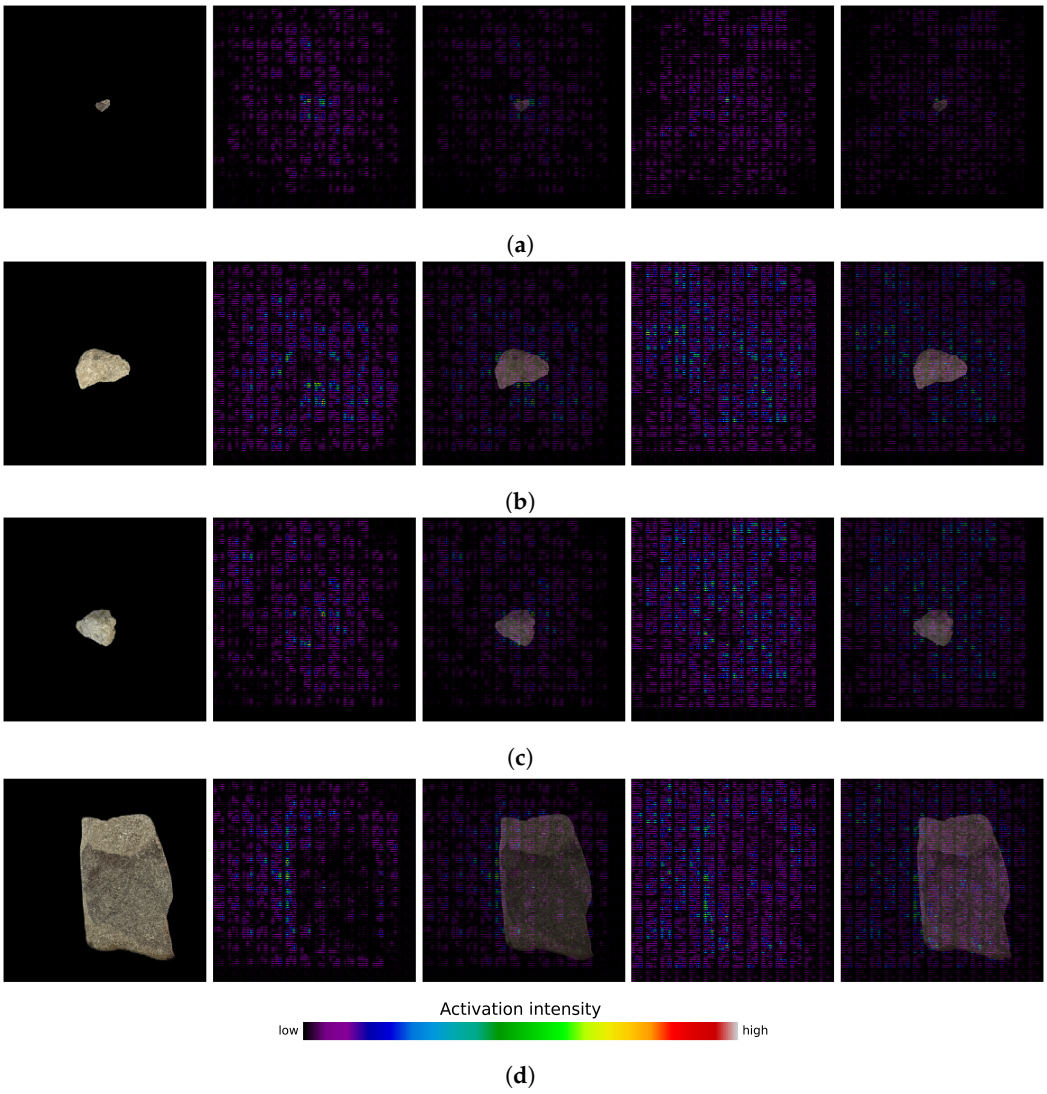


Figure 5. Saliency maps for the classification head. For each subfigure, from left to right: (1) input image; (2) saliency map model 2; (3) overlay saliency map and input image model 2; (4) saliency map model 11; and (5) overlay saliency map and input image model 11. (**a**) Particle from class 4–5.6 mm (correctly predicted by either model). (**b**) Particle from class 11.2–16 mm (falsely predicted by either model (16–22.4 mm)). (**c**) Particle from class 16–22.4 mm (falsely predicted by model 2 (11.2–16 mm)). (**d**) Particle from class 45–63 mm (correctly predicted by either model) and color map of the activation intensity for all subfigures.

3.2.2. Regression

For model 2, the RMSE for the entire test set equals 14.30 g. For model 11, it equals 16.69 g. Similarly, the RMSE for nearly all (true) classes is lower for model 11 compared to model 2, as can be seen in Table 3, with the exception of the coarse fraction, where especially the biggest class is predicted with larger error. Since model 11 was able to correctly predict all particles in the class 31.5 to 45 mm, it makes sense to analyze the RMSE for this class in more detail. For this predicted class, the RMSE equals 22.5 g (see Table 3), which is a mean difference of 29.7% compared to the mean weight. Assuming the residuals are approximately normally distributed would mean that 95% of the observations will fall

within ±45.0 g of the predicted values. It is also important to assess the error without as much influence of outliers, in particular due to the large variation in weight values for each of the classes. As such, the MAE has additionally been calculated for both models and for both groupings (i.e., true class and predicted class). The MAE equals 6.15 g for model 2 and 6.99 g for model 11. The results per group, again grouped for the true classes as well as the predicted classes, are shown in Table 4. These results show that the absolute error for the largest class is on average lower for both models compared to the RMSE values, suggesting the presence and influence of outliers. Similar patterns are also visible for the other classes. Additionally, consistent with the RMSE values, model 11 has much lower MAE values for the two lowest classes (2 to 5.6 mm) and the middle fractions (8 to 22.4 mm), where the error is up to 57% lower compared to model 2. Especially the 0.7 g (or 0.9–1.0 g when weighing outliers more heavily) absolute error on average for particles with a mean weight of 3.6 g is a promising first result that the weight of CDW particles could be predicted from 2D-RGB data.

Table 3. RMSEs of the final models per class, where (true class) refers to a grouping based on the true labels and (predicted class) on the predicted labels, respectively.

Class (mm)	Mean Weight ± σ (g)	RMSE Model 2 (True Class)	RMSE Model 2 (Predicted Class)	RMSE Model 11 (True Class)	RMSE Model 11 (Predicted Class)
2–4	0.04 ± 0.03	0.382	-	0.171	-
4–5.6	0.11 ± 0.05	0.316	0.322	0.118	0.125
5.6–8	0.44 ± 0.22	0.201	0.245	0.198	0.230
8–11.2	1.17 ± 0.48	0.655	0.634	0.540	0.462
11.2–16	3.58 ± 1.75	1.287	1.537	1.020	0.905
16–22.4	8.47 ± 3.78	6.214	6.153	2.810	2.664
22.4–31.5	26.11 ± 19.67	10.615	11.377	13.208	13.444
31.5–45	75.66 ± 23.26	28.071	25.487	43.318	22.511
45–63	104.25 ± 50.78	35.710	35.743	35.108	39.840

Table 4. Mean absolute errors of the final models per class, where (true class) refers to a grouping based on the true labels and (predicted class) on the predicted labels, respectively.

Class (mm)	MAE Model 2 (True Class)	MAE Model 2 (Predicted Class)	MAE Model 11 (True Class)	MAE Model 11 (Predicted Class)
2–4	0.381	-	0.170	-
4–5.6	0.312	0.317	0.094	0.099
5.6–8	0.143	0.173	0.159	0.188
8–11.2	0.518	0.491	0.374	0.332
11.2–16	1.026	1.146	0.797	0.714
16–22.4	4.724	4.614	2.194	1.999
22.4–31.5	7.358	8.007	8.867	8.843
31.5–45	22.439	21.381	37.308	20.288
45–63	27.864	28.446	28.450	33.546

As for most classes, both the RMSE and the MAE seem relatively high, so it makes sense to compare these values to the standard deviation for each class (see Table 3). From this comparison, it becomes clear that most of the errors fall within one standard deviation from the class mean. Especially interesting are the predictions for the classes 11.2 to 16 mm, 22.4 to 31.5 mm and 45 to 63 mm, where all error values for both models fall within one standard deviation from the mean. Moreover, when looking at the MAE, besides the two smallest classes, for model 2, the predictions for two classes—namely 8 to 11.2 mm and 16 to 22.4 mm—are, on average, more than one standard deviation off. This also holds for the

two smallest classes for model 11, as well as particles from 31.5 to 45 mm when grouped based on the true class.

Similarly to the analysis of classification behavior, saliency maps have been analyzed for the regression part of the models. Interestingly, for model 2, no activation is visible for the smallest particle (see Figure 6a), and the activation for the medium-sized particles only spans part of the image (see Figure 6b,c). Nonetheless, here too, for both models, it can be seen that the pixels representing the particles are less activated compared to the background. Additionally, for the largest particle, a clear peak in activation intensity is visible around the left contour of the particle (see Figure 6d).

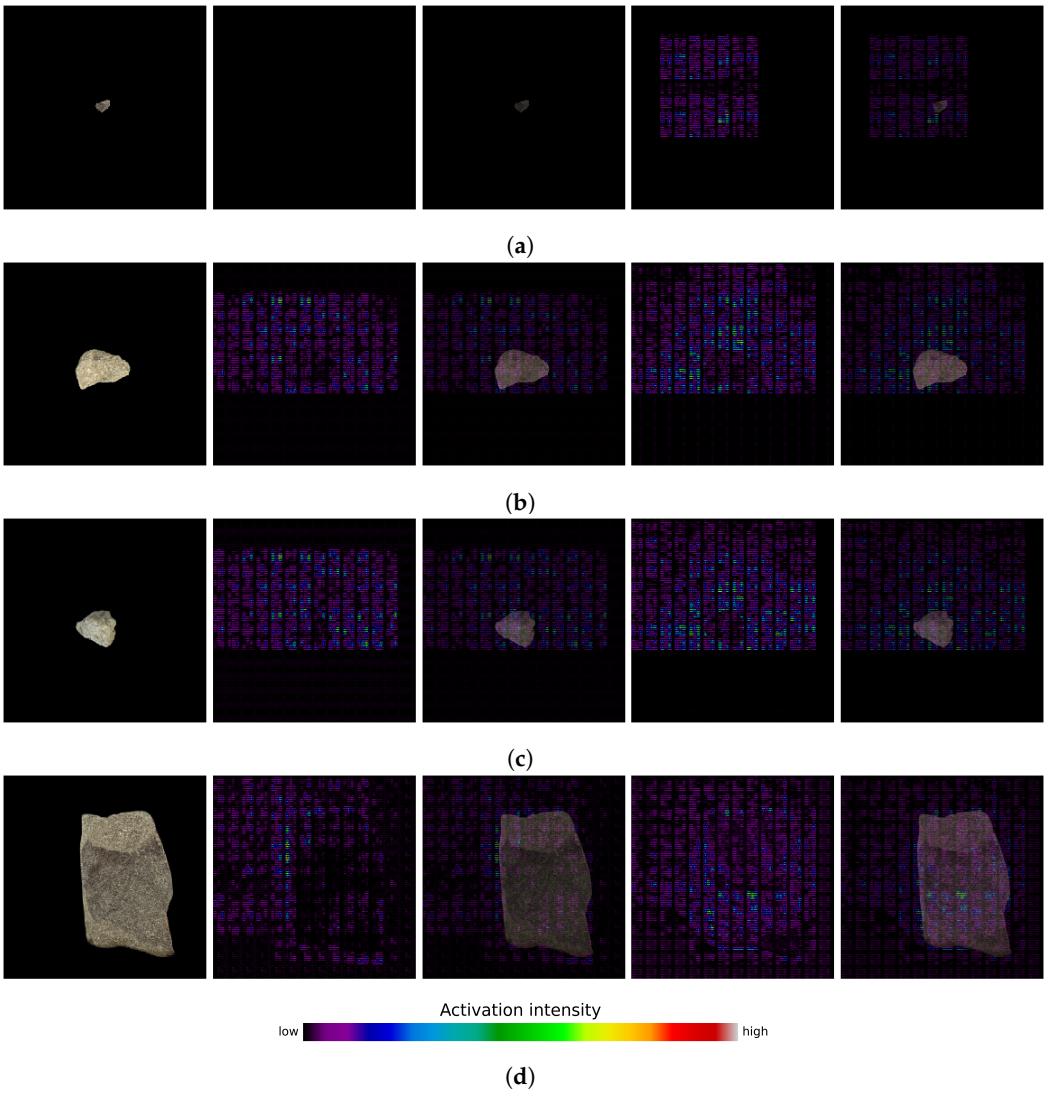


Figure 6. Saliency maps for the regression head. For each subfigure, from left to right: (1) input image; (2) saliency map model 2; (3) overlay saliency map and input image model 2; (4) saliency map model 11; and (5) overlay saliency map and input image model 11. (**a**) Particle with $m = 0.17$ g (model 2: 0.43 g; model 11: 0.07 g). (**b**) Particle with $m = 6.23$ g (model 2: 4.92 g; model 11: 7.31 g). (**c**) Particle with $m = 6.10$ g (model 2: 3.84 g; model 11: 3.36 g). (**d**) Particle with $m = 69.69$ g (model 2: 117.49 g; model 11: 161.61 g) and color map of the activation intensity for all subfigures.

As an indication of how well the models could predict a PSD, in Table 5, the percentage difference between the true and predicted aggregated weight for each class—grouped by the predicted class, is presented. These results indicate that the overall prediction error (i.e., difference between the aggregated true and predicted weight) is small for some of the classes. There is, however, visible difference between the two models. The low error

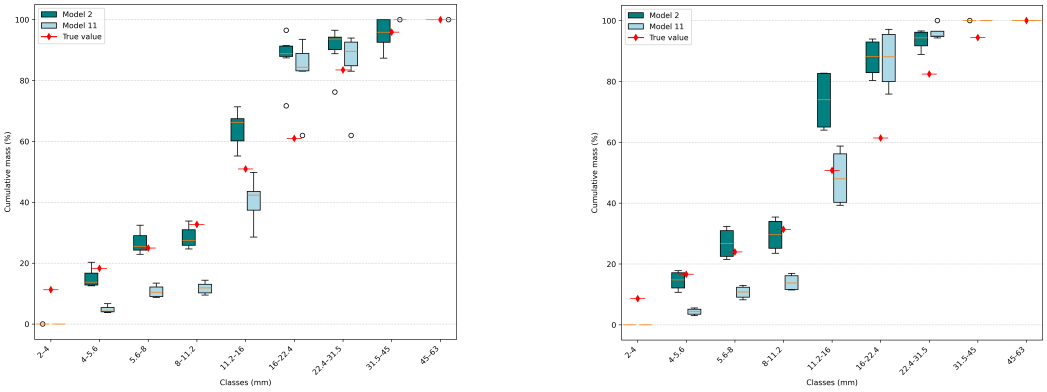
of 0.4% for model 2 on particles from 4 to 5.6 mm stands out in particular. Overall, the performance of model 11 seems better, with three errors under 2.0%, spanning the classes from 8 to 22.4 mm, and merely two errors above 10%. The errors of around 2% can be considered promising, given that the bounds against which the PSD is tested have ranges of 30–38 wt% for classes between 2 and 31.5 mm for unbound aggregates [19].

Table 5. Aggregated true versus predicted weight and the corresponding percentage difference. The corresponding classification accuracy can be extracted from the diagonals in the confusion matrices (see Figure 4c,d). Abbreviations: true = aggregated true weight, predicted = aggregated predicted weight, M2 = model 2, M11 = model 11.

Class (mm)	True (g)	Predicted M2 (g)	Predicted M11 (g)	Difference M2 (%)	Difference M11 (%)
2–4	0.2	1.7	0.9	40.3	32.5
4–5.6	5.9	22.2	9.2	28.9	10.6
5.6–8	17.7	17.4	13.4	0.4	7.0
8–11.2	46.8	35.7	50.4	6.8	1.8
11.2–16	143.3	120.1	150.3	4.4	1.2
16–22.4	338.6	201.9	323.0	12.7	1.2
22.4–31.5	835.5	885.3	1001.1	1.4	4.5
31.5–45	1588.9	1886.2	2350.8	4.3	9.7
45–63	3231.9	2954.6	3713.2	2.2	3.5

3.3. Performance on Full-Scale Plant Data

When comparing the predicted cumulative wt% distributions based on the models' classifications and weight predictions with the true PSDs acquired from the sieve analyses, visualized in Figure 7, it can be seen that model 2 is able to capture the cumulative trend for the smallest classes, up until the class with particles from 8 to 11.2 mm. However, this excludes the class 2 to 4 mm, which is largely embedded in the subsequent class, due to limited training (see Section 3.2.1). Looking at the results for the larger classes, an overestimation is especially visible for the particles ranging from 11.2 to 22.4 mm, which may stem from the relatively large weight prediction error for the class 16 to 22.4 mm and the misclassifications between these two classes, as indicated in Figure 4.



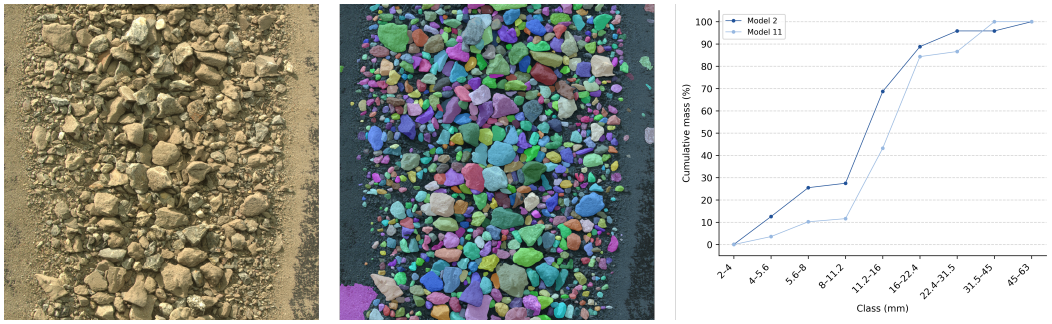
(**a**) (**b**)

Figure 7. Comparison of the true PSDs with the predicted values for both models. (**a**) The first sample taken for validation. (**b**) The second sample taken for validation.

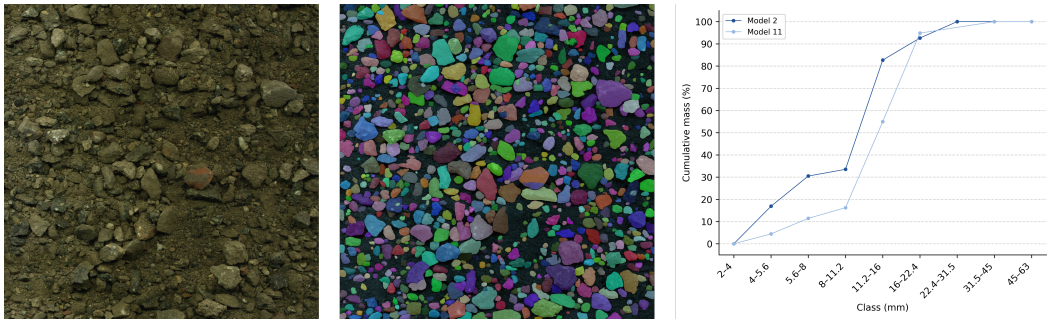
Interestingly, model 11 consistently underestimates the cumulative wt% of the smallest classes—albeit following the cumulative trend—but approaches the true share for the class 11.2 to 16 mm, in particular for the second sample (see Figure 7b). Furthermore, both models obtained different results from each image, visualized by the interquartile ranges (i.e., the boxes), bounds and sometimes outliers. In this context, it should, however, be noted that the models merely analyze particles on the top layer of the multilayer material

stream, meaning that there is likely to be some discrepancy between the PSD obtained by sieve analysis and the particles captured by the RGB sensor and segmentation procedure. Additionally, due to the practical constraints, there is no true PSD for a singular image available, but instead images within the time stamp range of the sample are aggregated for comparison.

In Figure 8, the first image and the corresponding segmentation map as well as the predicted PSDs for each of the samples is shown. This indicates which particles are included in the prediction of the PSD and what the predicted PSD of the corresponding image looks like. In the segmentation colormaps, it is clear that many of the small particles are not distinguished by the segmentation model, which—as described in Section 2.2.5—introduces another source of uncertainty that complicates the comparison of the PSD acquired from the sieve analysis compared to the one predicted by either model. Furthermore, the examples show that even though the image illumination can change during outside operation, both the segmentation and the PSD prediction parts seem to be relatively robust to these changes.



(**a**)



(**b**)

Figure 8. Examples of raw images (left), the segmentation process in the form of color maps highlighting the segmented particles (middle) and the predicted cumulative wt% distribution (right). (**a**) The first recorded image from sample 1. (**b**) The first recorded image from sample 2.

3.4. Limitations and Future Work

Since this work focused on the development of the CDW-MT-CNN model as a novel architecture for predicting the particle size distribution and investigating its feasibility to predict a particle's weight from 2D-RGB data while maintaining high classification performance and at the same time takes into account practical prerequisites, several starting points for further research are provided based on the remaining limitations.

First, the size of the data set in combination with the high variability of the particle weights is minimal, as is indicated by the large errors for some classes. We used a combination of data augmentation techniques for the creation of a second, extended data set to mitigate this limitation, which seems effective for most classes. However, to further optimize the predictive performance, for both classification and regression, a more extensive data set would be beneficial. In addition to creating a larger data set for this particular target fraction, it would be useful to create data sets with different target frac-

tions so that models can be trained (e.g., with transfer learning) and configured depending on the desired target fraction, which has high practical relevance. Related to this is the consideration that our data set cannot possibly embed all variations present in comminuted CDW material streams. However, given that the validation data are completely unseen and stem from sampled material collected in the time span of several months as well as different sampling campaigns, the results are indicative of the model performance on other unbound RCA material streams with similar compositions (i.e., mostly concrete and brick particles and including some tile parts, all with sizes of at most 63 mm) in at least Germany and possibly several other west-European countries such as the Netherlands. For further research on the generalizability of the model and potential systematic errors related to the reliance on the empirical relationships between visual features and particle weight, it would be valuable to investigate the performance on different compositions in terms of material type or size range in more detail and, for example, to assess to what extent transfer learning or continuous learning may be beneficial for its generalizability. An extension of such research could focus on batch-dependent corrections to solve potential inconsistencies in error propagation during monitoring in a pilot- or full-scale plant, for instance, on the basis of an in-depth simulation analysis.

Second, the error embedded in the prediction of the particle size distributions with the quality monitoring pipeline stems from five kinds of error and uncertainty, of which some are aleatoric (i.e., cannot be reduced). This regards the sieving process and extreme vibrations as well as different bulk heights slightly changing the distance from sensor to particle during operation. The other errors could be improved with further optimization of the used models, namely by improving the segmentation performance of ParticleSAM and the predictive performance—especially in terms of its weight prediction—of the proposed CDW-MT-CNN. The CDW-MT-CNN architecture can for instance be optimized by conducting an in-depth ablation study but also by (re)training on a bigger data set. Related to this, the results of the full-scale plant examples presented in this work show the importance and difficulty of developing suitable and sound methods to validate quality monitoring systems on pilot- and full-scale plants. Currently, no verified methods exist to extract the true particle size distribution (or other material characteristics) from a batch that exactly matches one or multiple images processed by the quality monitoring system. As such, further research could focus on investigating ways of how this could be achieved.

As indicated in the introduction, the PSD is not the only material quality factor during CDW comminution. Different factors may have different importance in the various countries. Therefore, additional studies could also focus on the extension of the presented solution, for instance, by adding an additional head for the classification of particle form.

4. Conclusions

Achieving higher transparency of the material specifications of processed CDW material is essential for boosting the use of CDW recycled aggregates in high-quality applications. One crucial specification is the particle size distribution, which comprises a particle classification in terms of size and the cumulative weight percentage of the particles contained in these particular classes. A major problem exists, however, in the translation from 2D (or 3D) data to accurate weight approximation and thus accurate PSDs. As such, in this work, we propose a novel CNN-based deep learning model, namely CDW-MT-CNN, which is able to classify the particles and their weight simultaneously based on an RGB-image in 54 ms per image. To develop this model, we manually photographed and weighed 1486 CDW particles to develop a realistic data set and further increased the size of the training set using different augmentation techniques. Based on this data set, 12 different configurations of the CDW-MT-CNN architecture have been tested on 2 different seeds.

The best model trained on the original data set (model 2) is able to achieve 82% accuracy with a nMCC-score of 0.80 for the classification and an overall MAE of 6.15. The model trained on the augmented data has overall slightly worse performance: 79% classification accuracy and 6.99 weight prediction error. However, augmentation seems beneficial for the weight prediction of the middle fractions (i.e., 5.6 to 22.4 mm), suggesting that augmentation can be a suitable technique to mitigate data labeling limitations for CDW-related data set creation.

Results of the full-scale plant experiment further indicate lower performance for the largest particle size classes, which is also shown in the misclassifications on the labeled data set. However, model 2 in particular shows the feasibility of predicting the PSD with close approximation to the true distribution for particles ranging from 4 to 11.2 mm. Moreover, these experiments have shown the difficulty of validating a quality monitoring system on a full-scale plant due to the infeasibility of acquiring exact true distributions for each individual image and the additional uncertainties that are embedded in full-scale plants, such as severe vibrations and throughput fluctuations.

Nonetheless, this work shows that the CDW-MT-CNN architecture is able to predict the particle sizes with high correctness and the particle weight for many of those classes within one standard deviation from the mean, which provides a valuable basis for further optimization of this architecture. Furthermore, using a praxis-oriented approach, a focus was put on creating a lightweight and fast model. With average inference times of 54 ms per image, this too is a suitable basis [RQ1]. The architecture also shows to an extent decent results for the full-scale plant experiments, but further validation on the practical levels should be conducted. Furthermore, the model can be used as a part of the quality monitoring system, but for inline monitoring in a full-scale plant, the combined quality monitoring system should ideally process with a frequency of one image per second to monitor the entire stream, which is not yet achievable with the current inference time. Nonetheless, further optimization in terms of inference speed and predictive performance is expected to provide models with a performance that is able to support the manual quality assessments and therewith the improved recycling of CDW for recycled aggregates in high-quality applications [RQ2].

Author Contributions: Conceptualization, L.G., K.R. and K.G.; methodology, L.G.; software, L.G.; validation, L.G.; formal analysis, L.G.; investigation, L.G. and S.O.; resources, L.G.; data curation, L.G.; writing—original draft preparation, L.G. and S.O.; writing—review and editing, L.G. and K.R.; visualization, L.G.; supervision, K.G.; project administration, K.R.; funding acquisition, K.R. and K.G. All authors have read and agreed to the published version of the manuscript.

Funding: This work was funded by the German Federal Ministry of Education and Research (BMBF), now the German Federal Ministry of Research, Technology and Space (BMFTR), within the program "Digital GreenTech" under the project KIMBA (grant no. 2WDG1693D). Open access funding was provided by the RWTH Aachen University Open Access Publication Fund. The responsibility for the content of this publication lies with the authors.

Data Availability Statement: The data sets presented in this article are not readily available because the data are part of an ongoing study. Requests to access the data sets should be directed to the corresponding author.

Acknowledgments: The authors would like to extend their appreciation to MAV GmbH and KLEEMANN GmbH for supporting this study.

Conflicts of Interest: The authors declare no conflicts of interest.

Abbreviations

The following abbreviations are used in this manuscript:

CDW	Construction and demolition waste
CDW-MT-CNN	Construction and building waste multitask-convolutional neural network
CEL	Cross-entropy loss
CMOS	Complementary metal-oxide-semiconductor
CNN	Convolutional neural network
CPU	Central processing unit
DSNU	Dark signal non-uniformity
GPS	Global positioning system
GPU	Graphics processing unit
MAE	Mean absolute error
MCC	Matthews correlation/Phi coefficient
MRI	Magnetic resonance imaging
PRNU	Photo response non-uniformity
PSD	Particle size distribution
RC	Recycled concrete
ReLU	Rectified linear unit
RGB	Red-green-blue
RMSE	Root mean square error
TRL	Technology readiness level
wt%	Percentage by weight
2D	Two-dimensional
3D	Three-dimensional

References

1. Eurostat. Generation of Waste by Waste Category, Hazardousness and NACE Rev. 2 Activity. Available online: https://ec.europa.eu/eurostat/databrowser/view/ENV_WASGEN__custom_3064907/default/table?lang=en (accessed on 10 November 2025).
2. European Commission. *EU Construction Sector: In Transition Towards a Circular Economy*; Technical report; European Construction Sector Observatory: Brussels, Belgium 2019.
3. E3G. *Renovate2Recover: How Transformational Are the National Recovery Plans for Buildings Renovation?*; Technical report; E3G: Brussels, Belgium 2021.
4. Global Property Guide News Team. Germany's Housing Market Remains Strong. Available online: https://www.globalpropertyguide.com/news-germanys-housing-market-remains-strong-4271 (accessed on 20 November 2025).
5. Bundesministerium für Wohnen, Stadtentwicklung und Bauwesen. Maßnahmenpaket der Bundesregierung. Available online: https://www.bmwsb.bund.de/SharedDocs/topthemen/DE/Massnahmenpaket-bauen/massnahmenpaket-artikel.html (accessed on 10 November 2025).
6. Statistisches Bundesamt. Bauschuttaufbereitungsanlagen: Deutschland, Jahre, Abfallarten. Available online: https://www-genesis.destatis.de/datenbank/online/statistic/32141/table/32141-0002 (accessed on 10 November 2025).
7. Tam, V.W.; Soomro, M.; Evangelista, A.C.J. A review of recycled aggregate in concrete applications (2000–2017). *Constr. Build. Mater.* **2018** , *172*, 272–292. [CrossRef]
8. Choudhary, J.; Kumar, B.; Gupta, A. Utilization of solid waste materials as alternative fillers in asphalt mixes: A review. *Constr. Build. Mater.* **2020**, *234*, 117271. [CrossRef]
9. Göbbels, L.; Feil, A.; Raulf, K.; Greiff, K. Current State of the Art and Potential for Construction and Demolition Waste Processing: A Scoping Review of Sensor-Based Quality Monitoring and Control for In- and Online Implementation in Production Processes. *Sensors* **2025**, *25*, 4401. [CrossRef]
10. Kandlbauer, L.; Khodier, K.; Ninevski, D.; Sarc, R. Sensor-based Particle Size Determination of Shredded Mixed Commercial Waste based on two-dimensional Images. *Waste Manag.* **2021**, *120*, 784–794. [CrossRef]
11. Di Maria, F.; Bianconi, F.; Micale, C.; Baglioni, S.; Marionni, M. Quality assessment for recycling aggregates from construction and demolition waste: An image-based approach for particle size estimation. *Waste Manag.* **2016**, *48*, 344–352. [CrossRef]

12. Kroell, N.; Thor, E.; Göbbels, L.; Schönfelder, P.; Chen, X. Deep learning-based prediction of particle size distributions in construction and demolition waste recycling using convolutional neural networks on 3D laser triangulation data. *Constr. Build. Mater.* **2025**, *466*, 140214. [CrossRef]
13. Bilodeau, M.; Gouveia, D.; Demers, A.; Di Feo, A. 3D free fall rock size sensor. *Miner. Eng.* **2020**, *148*, 106169. [CrossRef]
14. Shimizu, H.; Fukuda, T.; Yabuki, N. Deep-learning Point Cloud Classification for Estimating the Weight of Single-material Construction and Demolition Waste of Unknown Shape. In Proceedings of the 41st Conference on Education and Research in Computer Aided Architectural Design in Europe (eCAADe 2023), Graz, Austria, 20–22 September 2023; pp. 609–618. [CrossRef]
15. Di Maria, A.; Eyckmans, J.; Van Acker, K. Downcycling versus recycling of construction and demolition waste: Combining LCA and LCC to support sustainable policy making. *Waste Manag.* **2018**, *75*, 3–21. [CrossRef] [PubMed]
16. Kranert, M. (Ed.) *Einführung in die Kreislaufwirtschaft: Planung, Recht, Verfahren*, 6th ed.; Springer Vieweg: Wiesbaden, Germany, 2024. [CrossRef]
17. Göbbels, L.; Kroell, N.; Raulf, K. Towards an improvement of construction and demolition waste recycling: Investigating the feasibility of using AI-based quality control using sensor-based monitoring of particle size distributions. In *Global Guide of the Filtration and Separation Industry 2024–2026*; Vulkan Verlag GmbH: Essen, Germany, 2025; pp. 124–130.
18. *DIN EN 12620:2008-07*; Aggregates for Concrete. Deutsches Institut für Normung e.V.: Berlin, Germany, 2008. [CrossRef]
19. *DIN EN 13285*; Unbound Mixtures Specifications. Deutsches Institut für Normung e.V.: Berlin, Germany, 2018. [CrossRef]
20. Alimi, K.; Jin, R.; Nguyen, N.; Nguyen, Q.; Hosking, L. Exploring artificial intelligence applications in construction and demolition waste management: A review of existing literature. *J. Sci. Transp. Technol.* **2025**, *5*, 104–136. [CrossRef]
21. Hussain, R.; Alican Noyan, M.; Woyessa, G.; Retamal Marín, R.R.; Antonio Martinez, P.; Mahdi, F.M.; Finazzi, V.; Hazlehurst, T.A.; Hunter, T.N.; Coll, T.; et al. An ultra-compact particle size analyser using a CMOS image sensor and machine learning. *Light. Sci. Appl.* **2020**, *9*, 21. [CrossRef] [PubMed]
22. Idroas, M.; Najib, S.; Ibrahim, M. Imaging particles in solid/air flows using an optical tomography system based on complementary metal oxide semiconductor area image sensors. *Sens. Actuators B Chem.* **2015**, *220*, 75–80. [CrossRef]
23. Bittelli, M.; Pellegrini, S.; Olmi, R.; Andrenelli, M.C.; Simonetti, G.; Borrelli, E.; Morari, F. Experimental evidence of laser diffraction accuracy for particle size analysis. *Geoderma* **2022**, *409*, 115627. [CrossRef]
24. Varli, C.; Göbbels, L.; Raulf, K.; Mirbach, B.; Häberle, S.; Lutz, M.; Höhn, J.; Dehnen, G. *Verbundprojekt KIMBA-KI-Basierte Prozesssteuerung und Automatisiertes Qualitätsmanagement im Recycling von Bau- und Abbruchabfällen durch Sensorbasiertes Inline-Monitoring von Korngrößenverteilungen: Sachbericht zum Verwendungsnachweis in der Fördermaßnahme Digital GreenTech-Umwelttechnik trifft Digitalisierung*; Technical report; Technische Informationsbibliothek: Hannover, Germany, 2026 . [CrossRef]
25. Kronenwett, F.; Maier, G.; Leiss, N.; Gruna, R.; Thome, V.; Längle, T. Sensor-based characterization of construction and demolition waste at high occupancy densities using synthetic training data and deep learning. *Waste Manag. Res. J. Sustain. Circ. Econ.* **2024**, *42*, 788–796. [CrossRef]
26. Beskopylny, A.N.; Shcherban', E.M.; Stel'makh, S.A.; Razveeva, I.; Mailyan, A.L.; Elshaeva, D.; Chernil'nik, A.; Nikora, N.I.; Onore, G. Crushed Stone Grain Shapes Classification Using Convolutional Neural Networks. *Buildings* **2025**, *15*, 1982. [CrossRef]
27. *DIN EN 13242*; Aggregates for Unbound and Hydraulically Bound Materials for Use in Civil Engineering Work and Road Construction. Deutsches Institut für Normung e.V.: Berlin, Germany, 2008.
28. *DIN EN 933-1*; Tests for Geometrical Properties of Aggregates—Part 1: Determination of Particle Size Distribution—Sieving Method. Deutsches Institut für Normung e.V.: Berlin, Germany, 2021. [CrossRef]
29. Kroell, N.; Schönfelder, P.; Chen, X.; Johnen, K.; Feil, A.; Greiff, K. Sensorbasierte Vorhersage von Korngrößenverteilungen durch Machine Learning Modelle auf Basis von 3D- Lasertriangulationsmessungen. In Proceedings of the 11. DGAW-Wissenschaftskongress "Abfall- und Ressourcenwirtschaft", Dresden, Germany, 17 March 2022.
30. Pacheco, J.; De Brito, J. Recycled Aggregates Produced from Construction and Demolition Waste for Structural Concrete: Constituents, Properties and Production. *Materials* **2021**, *14*, 5748. [CrossRef] [PubMed]
31. Shorten, C.; Khoshgoftaar, T.M. A survey on Image Data Augmentation for Deep Learning. *J. Big Data* **2019**, *6*, 60. [CrossRef]
32. Wodzinski, M.; Kwarciak, K.; Daniol, M.; Hemmerling, D. Improving deep learning-based automatic cranial defect reconstruction by heavy data augmentation: From image registration to latent diffusion models. *Comput. Biol. Med.* **2024**, *182*, 109129. [CrossRef] [PubMed]
33. Perez, L.; Wang, J. The Effectiveness of Data Augmentation in Image Classification using Deep Learning. *arXiv* **2017**, arXiv:1712.04621. [CrossRef]
34. Mumuni, A.; Mumuni, F. Data augmentation: A comprehensive survey of modern approaches. *Array* **2022**, *16*, 100258. [CrossRef]
35. Islam, T.; Hafiz, M.S.; Jim, J.R.; Kabir, M.M.; Mridha, M. A systematic review of deep learning data augmentation in medical imaging: Recent advances and future research directions. *Healthc. Anal.* **2024**, *5*, 100340. [CrossRef]
36. Howard, A.; Sandler, M.; Chu, G.; Chen, L.C.; Chen, B.; Tan, M.; Wang, W.; Zhu, Y.; Pang, R.; Vasudevan, V.; et al. Searching for MobileNetV3. *arXiv* **2019**, arXiv:1905.02244. [CrossRef]

37. Krizhevsky, A.; Sutskever, I.; Hinton, G.E. ImageNet classification with deep convolutional neural networks. *Commun. ACM* **2017**, *60*, 84–90. [CrossRef]
38. Wang, H.; Raj, B. On the Origin of Deep Learning. *arXiv* **2017**, arXiv:1702.07800. [CrossRef]
39. Simonyan, K.; Zisserman, A. Very Deep Convolutional Networks for Large-Scale Image Recognition. *arXiv* **2015**, arXiv:1409.1556. [CrossRef]
40. Szegedy, C.; Liu, W.; Jia, Y.; Sermanet, P.; Reed, S.; Anguelov, D.; Erhan, D.; Vanhoucke, V.; Rabinovich, A. Going deeper with convolutions. In Proceedings of the 2015 IEEE Conference on Computer Vision and Pattern Recognition (CVPR), Boston, MA, USA, 7–12 June 2015; pp. 1–9. [CrossRef]
41. Chhapariya, K.; Benoit, A.; Buddhiraju, K.M.; Kumar, A. A Multitask Deep Learning Model for Classification and Regression of Hyperspectral Images: Application to the large-scale dataset. *arXiv* **2024**, arXiv:2407.16384. [CrossRef]
42. Padmapriya, K.; Periyathambi, E. Joint classification and regression with deep multi task learning model using conventional based patch extraction for brain disease diagnosis. *PeerJ Comput. Sci.* **2024**, *10*, e2538. [CrossRef] [PubMed]
43. Wilson, A.C.; Roelofs, R.; Stern, M.; Srebro, N.; Recht, B. The Marginal Value of Adaptive Gradient Methods in Machine Learning. In Proceedings of the Advances in Neural Information Processing Systems (NIPS 2017), Long Beach, CA, USA, 4–9 September 2017; pp. 4148–4158.
44. Stoica, P.; Babu, P. Pearson–Matthews correlation coefficients for binary and multinary classification. *Signal Process.* **2024**, *222*, 109511. [CrossRef]
45. Branco, P.; Torgo, L.; Ribeiro, R. A Survey of Predictive Modelling under Imbalanced Distributions. *arXiv* **2015**, arXiv:1505.01658. . [CrossRef]
46. Zhou, Y.; Thielmann, P.; Chamoli, A.; Mirbach, B.; Stricker, D.; Raphael Rambach, J. ParticleSAM: Small Particle Segmentation for Material Quality Monitoring in Recycling Processes. *arXiv* **2025**, arXiv:2508.03490. [CrossRef]

Disclaimer/Publisher's Note: The statements, opinions and data contained in all publications are solely those of the individual author(s) and contributor(s) and not of MDPI and/or the editor(s). MDPI and/or the editor(s) disclaim responsibility for any injury to people or property resulting from any ideas, methods, instructions or products referred to in the content.